# How can renewable hydrogen compete with diesel in public transport? Robust design optimization of a hydrogen refueling station under techno-economic and environmental uncertainty*

Diederik Coppitters[a,b,c,*], Kevin Verleysen[b,c], Ward De Paepe[a], Francesco Contino[d]

[a] *Thermal Engineering and Combustion Unit, University of Mons (UMONS), Place du parc 20, 7000 Mons, Belgium*
[b] *Fluid and Thermal Dynamics (FLOW), Vrije Universiteit Brussel, Pleinlaan 2, 1050 Brussels, Belgium*
[c] *Combustion and Robust Optimization Group (BURN),Vrije Universiteit Brussel (VUB) and Université Libre de Bruxelles (ULB), 1050 Brussels, Belgium*
[d] *Institute of Mechanics, Materials and Civil Engineering (iMMC), Université catholique de Louvain (UCLouvain), Place du Levant, 2, 1348 Louvain-la-Neuve*

**Abstract**

Heavy-duty transport represents nearly 6% of the greenhouse gas emissions in Europe. Renewable hydrogen is a potential option to decarbonize heavy-duty transport, such as buses. Renewable hydrogen for buses promises excellent environmental performance, at the expense of a higher fuel cost, as opposed to a diesel-powered bus fleet. Despite the inherent uncertainty, feasibility studies in this framework generally assume deterministic techno-economic and environmental parameters, which can lead to a suboptimal performance that is sensitive to the random environment. To provide robust design alternatives, we applied robust design optimization on a wind- and solar-powered hydrogen refueling system and a hydrogen- and diesel-powered bus fleet, to optimize the Levelized Cost Of Driving (LCOD) and Carbon Intensity (CI), subject to technical, economic and environmental uncertainties. A fully diesel-powered bus fleet achieves the optimized LCOD mean of 1.24 €/km, but it results in the worst LCOD standard

*The short version of the paper was presented at 100%RES, October 29-30, Pisa. This paper is a substantial extension of the short version of the conference paper.

*Corresponding author
*Email address:* diederik.coppitters@umons.ac.be (Diederik Coppitters)

deviation (0.11 €/km), CI mean (1.33 $kg_{CO_2,eq}$/km) and CI standard deviation (0.075 $kg_{CO_2,eq}$/km) among the optimized designs. To reduce the LCOD standard deviation, CI mean and CI standard deviation, part of the diesel-powered bus fleet is converted into hydrogen-powered buses and the renewable-powered hydrogen refueling station is scaled accordingly. Converting 54 % of the diesel-powered bus fleet into hydrogen-powered buses results in a decrease in LCOD standard deviation by 36 %, a decrease in CI mean by 46 % and a decrease in CI standard deviation by 51 %, at the expense of an increase in LCOD mean by only 11 %. Future work will focus on the integration of full-electric buses.

*Keywords:* Renewable hydrogen, Carbon intensity, hydrogen-powered buses, robust design optimization, techno-economic and environmental uncertainty.

---

## 1. Introduction

Heavy-duty vehicles are significant emitters of $CO_2$ (6 % of the global energy-related emissions) [1]. For that reason, the reduction of emissions from public buses is actively researched [2]. Significant emission reductions can be achieved by replacing diesel-powered buses with battery-electric buses [3] or Fuel Cell Electric Buses (FCEB), fueled by renewable hydrogen [4, 5]. With a refueling time similar to traditional diesel-powered buses (i.e., 10 min, as opposed to 3 h - 5 h for electric buses) and promising performance over extended driving ranges (i.e., 250 km) [6], FCEB achieve significant interest across Europe, with over 90 FCEB deployed in 2018 [7].

The hydrogen can be produced by a renewable-powered Hydrogen Refueling Station (HRS), which corresponds to an Integrated Energy System (IES) [8] as it couples power and mobility in the system [9]. Indeed, an IES couples different sectors (i.e., power, heat, mobility) and evaluates the interactions among different technologies, energy vectors and needs (i.e., whole-energy system approach) [10]. IES are well-documented in the literature: Fattahi et al. [11] reviewed nineteen IES models and identified the main capabilities and shortcomings of these models, whereafter potential solutions to these shortcomings

**Nomenclature**

| | | | |
|---|---|---|---|
| $C_{\text{diesel,a}}$ | annualized diesel cost, € | $\text{OPEX}_{\text{a}}$ | annualized operational expense, € |
| $C_{\text{grid,a}}$ | annualized grid cost, € | $p$ | polynomial degree |
| $\text{CAPEX}_{\text{a}}$ | annualized capital expense, € | $P$ | power, W |
| $C_{\text{repl,a}}$ | annualized replacement costs, € | PCE | Polynomial Chaos Expansion |
| CI | Carbon Intensity, $\text{kg}_{\text{CO}_2,\text{eq}}$/km | PEM | Proton Exchange Membrane |
| CRF | Capital Recovery Factor | PV | PhotoVoltaic |
| $D$ | distance travelled, km | $R$ | resistance, Ω |
| $d$ | stochastic dimension | RDO | Robust Design Optimization |
| $F$ | Faraday constant, 96 485 C/mol | $T$ | temperature, K |
| FCEB | Fuel Cell Electric Buses | $U$ | voltage, V |
| GHG | GreenHouse Gas | UQ | Uncertainty Quantification |
| $\text{GHG}_{\text{comp,a}}$ | annualized GreenHouse Gas Emissions components, $\text{kg}_{\text{CO}_2,\text{eq}}$ | $\eta$ | efficiency |
| | | $\xi$ | independent random parameter |
| $\text{GHG}_{\text{diesel,a}}$ | annualized GreenHouse Gas Emissions diesel, $\text{kg}_{\text{CO}_2,\text{eq}}$ | $\Psi$ | orthogonal polynomial |
| | | act | activation |
| $\text{GHG}_{\text{grid,a}}$ | annualized GreenHouse Gas Emissions grid, $\text{kg}_{\text{CO}_2,\text{eq}}$ | con | concentration |
| | | L | photogenerated |
| HRS | Hydrogen Refueling Station | oc | open-circuit |
| $I$ | current, A | ohm | ohmic |
| $k$ | specific heat ratio | sh | shunt |
| LCOD | Levelized Cost Of Driving, €/km | s | series |
| $\dot{m}$ | mass flow rate, kg/s | th | thermal |
| $\dot{n}$ | molar flow rate, mol/s | | |

are suggested. Collins et al. [12] reviewed methodologies to address short term variations in IES, due to the increased penetration of intermittent renewable energy sources. Wang et al. [13] summarized the main research practices on Integrated Energy Distribution Systems, explored the main coupling mechanisms and identified, among others, joint planning optimization control and security analysis as the main issues. Ruiming et al. [14] incorporated hydrogen storage in the multi-objective optimization of an IES and proposed a solution that re-

Table 1: The cost of hydrogen production using solar photovoltaic and wind turbines is higher than for the traditional $CO_2$-emitting alternatives.

| type | cost range [€/$kg_{H_2}$] | Ref. |
|---|---|---|
| solar photovoltaic hydrogen | 4.80 - 19.31 | [18] |
| | 9.29 - 12.48 | [19] |
| | 15.5 - 22.5 | [20] |
| wind hydrogen | 4.89 - 5.00 | [18] |
| | 4.40 - 4.81 | [21] |
| | 1.16 - 32.83 | [22] |
| steam methane reforming | 1.73 - 1.88 | [18] |
| methane pyrolysis | 1.32 - 1.41 | [18] |
| coal gasification | 1.11 - 1.35 | [18] |

duced the carbon emissions by 3.5 %, at the expense of a 2.8 % increase in the operating costs.

The production of hydrogen in a renewable-powered HRS is not entirely carbon-free: Spath et al. [15] and Burkhardt et al. [16] quantified the GHG emission for a wind-powered HRS and they present values of $0.97\,kg_{CO_2,eq}/kg_{H_2}$ and $1.92\,kg_{CO_2,eq}/kg_{H_2}$ (i.e., $29\,g_{CO_2,eq}$/kWh and $58\,g_{CO_2,eq}$/kWh), respectively. Nevertheless, the GHG emissions are significantly lower compared to the well-to-wheel emission factor for diesel, quantified at $326\,g_{CO_2,eq}$/kWh [17]. Despite the clear environmental advantage, the cost of renewable hydrogen production using PhotoVoltaic (PV) arrays and wind turbines remains relatively high (Table 1). In comparison, the $CO_2$-emitting hydrogen production alternatives are more beneficial in terms of economic performance [18].

When evaluating the techno-economic and environmental performance of a renewable-powered HRS, the model parameters are often assumed deterministic. However, parameters such as the interannual variability of the solar irradi-

ance, the wind speed and the carbon intensity of grid electricity are subject to uncertainty. Such techno-economic and environmental uncertainties affect the system performance and can lead to biased conclusions [23]. To address these uncertainties when optimizing a renewable-powered HRS, stochastic optimization methods can be applied [24]. In this framework, stochastic programming is a scenario-based approach in which the expected value of the system performance is optimized, subject to probabilistic input uncertainties [25, 26]. Alternatively, robust optimization provides optimized solutions under the worst-case combination of the input parameters values, which are defined by interval uncertainty [27]. In other fields, such as structural mechanics [28] and aerospace engineering [29], Robust Design Optimization (RDO) gained attention over the last decade [30]. RDO considers probabilistic uncertainties at the model inputs and optimizes both the expected performance (i.e., the mean) and the variability of that performance (i.e., the standard deviation) [31]. Hence, by considering the standard deviation of the quantity of interest as an optimization objective, RDO aims at providing designs that are less sensitive to the random environment (i.e., the design with the lowest standard deviation is the robust design) [32]. Note that the reduced sensitivity towards uncertainty is achieved by modifying the design variables, as opposed to reducing the uncertainty related to the random environment. Bilel et al. [33] performed an RDO on a mechatronic system in a sewing machine and showed that the robust design reduced the variance on the motor current and its fluctuation by 67 % and 83 %, respectively, at the expense of a slight increase up to 3 % in the mean of the corresponding quantities of interest. De Paepe et al. [34] provided a robust design for a micro gas turbine by minimizing the relative standard deviation of the electrical efficiency and power output.

To perform RDO, an Uncertainty Quantification (UQ) method is required that quantifies the mean and standard deviation of the quantity of interest, for each design evaluated during the optimization procedure. Thus, to quantify the effect of techno-economic and environmental uncertainties on the performance of an HRS for each design, Monte Carlo simulation is an always-converging UQ

method [35]. However, due to its brute force approach, Monte Carlo simulation is computationally expensive ($10^4 - 10^5$ model evaluations to achieve accurate statistical moments) [36]. Computationally efficient alternatives include the construction of surrogate models, based on a reduced set of training samples (i.e., $10^2 - 10^3$ samples) [37]. Typical surrogate models for UQ include Gaussian Process Regression [38], Support Vector Machines [39], and Polynomial Chaos Expansion (PCE) [40]. Despite that PCE has been proven effective on similar hydrogen-based renewable energy systems [41, 42], the number of training samples under a conventional PCE truncation scheme scales exponentially with the number of uncertain parameters considered (i.e., the stochastic dimension) [40]. Consequently, conventional PCE suffers from the curse-of-dimensionality, which leads to computationally intractable problems when the stochastic dimension is high (i.e., more than 15 uncertain parameters). To tackle this issue, sparse alternatives to the conventional PCE scheme have been proposed, such as the Least Angle Regression approach by Blatman et al. [43] and the stepwise regression approach by Abraham et al. [44]. In the context of hydrogen-based systems, Coppitters et al. [45] used the stepwise regression approach to quantify the statistical moments on the levelized cost of electricity of a PV-battery-hydrogen system, improving the computational efficiency by 71 % compared to a conventional PCE.

In summary, design and feasibility studies on renewable-powered HRS indicate excellent environmental performance, at the expense of a higher cost. However, these studies assumed fixed parameters, which can lead to designs and conclusions that are sensitive to technical, economic and environmental uncertainties over the system lifetime. Therefore, we applied RDO on the design of a wind- and solar-powered HRS, considering a large set of technical, economic, and environmental uncertainties (39 in total). In addition to sizing the HRS component capacities, the bus fleet composition is an additional design variable. Through this design variable, the optimization algorithm configures the fraction of the bus fleet powered by hydrogen, while the remainder of the bus fleet is powered by conventional diesel. Consequently, the designs are op-

timized based on the expected performance (i.e., the mean) and the sensitivity of that performance (i.e., the standard deviation) to the technical, economic and environmental uncertainties. By considering these statistical moments as optimization objectives, this paper provides novel designs, least-sensitive towards the random environment, and highlights additional benefits in terms of robustness for hydrogen-powered heavy-duty transport. Section 2 provides the lay-out of the HRS, the adopted models for each component, the quantities of interest, the characterization of the uncertainties and the RDO algorithm. The optimized design characteristics for each quantity of interest and the results for a holistic RDO (i.e., considering all quantities of interest at once) are discussed in Section 3. The main messages of this paper are provided in Section 4. Finally, the parametric uncertainties are provided in Appendix A.

## 2. Method

In this section, the HRS is described and the component modelling is introduced. Thereafter, the quantities of interest are presented, followed by the RDO algorithm.

### *2.1. Hydrogen refueling station*

The mobility demand corresponds to a bus depot in Brussels, Belgium. At the bus depot, a typical amount of 40 buses [46] are stationed with an average utilisation rate of 250 km/bus/day [7]. The bus fleet can consist of hydrogen-powered buses (i.e., FCEB), diesel-powered buses or a mix of both.

To determine the refueling period for these buses, we adopted the daily bus refueling profile from the NewBusFuel project (Figure 1) [47]. This profile is based on 13 case studies for different HRS across Europe. Most refueling activities occur at night (i.e., 72 % of the bus fleet is refueled between 8 PM and 2 AM), when the bus service is reduced and most FCEB are available at the bus depot. On the one hand, reducing the refueling time increases the number of dispensers in parallel, as more FCEB need to be refueled in the same period. On

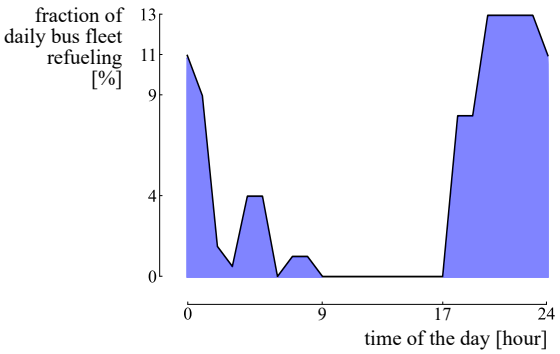


Figure 1: The refueling profile indicates the temporal distribution of the daily refueling of the Fuel Cell Electric Buses (FCEB). The refueling is performed in the evening and at night, between 5 PM and 9 AM, when the bus service is reduced and most buses are at the depot.

the other hand, extending the refueling time for the bus fleet increases the working hours of the personnel [47]. The dispensation pressure for FCEB is fixed at 350 bar, as opposed to 700 bar for hydrogen-powered cars, as buses allow carrying more volume than passenger cars. This reduced dispensing pressure lowers the HRS complexity (i.e., no cooling unit before dispensation), compression energy, system cost and improves reliability [47]. In a future where hydrogen-powered passenger vehicles are massively deployed, converting the dispensation pressure for FCEB to 700 bar can result in advantages related to uniformity of distribution systems. However, today and in the near future, 350 bar remains the state-of-the-art dispensation pressure for FCEB [47].

To fuel the FCEB, a renewable-powered HRS is considered (Figure 2). The power management strategy for the HRS aims at continuously complying with the hydrogen demand. During the refueling period, hydrogen is extracted from the storage tank. When the stored hydrogen is insufficient to meet the demand, the remaining hydrogen is produced instantaneously (i.e., cold start-up time: 5 min - 10 min; warm start-up time: below 10 s [48]) in the Proton Exchange Membrane (PEM) electrolyzer array, compressed in the compressor and dispensed. To power the PEM electrolyzer array and compressor, the available wind and solar power is called upon first. If the instantaneous solar and wind power does not comply with the power demand from the electrolyzer and com-

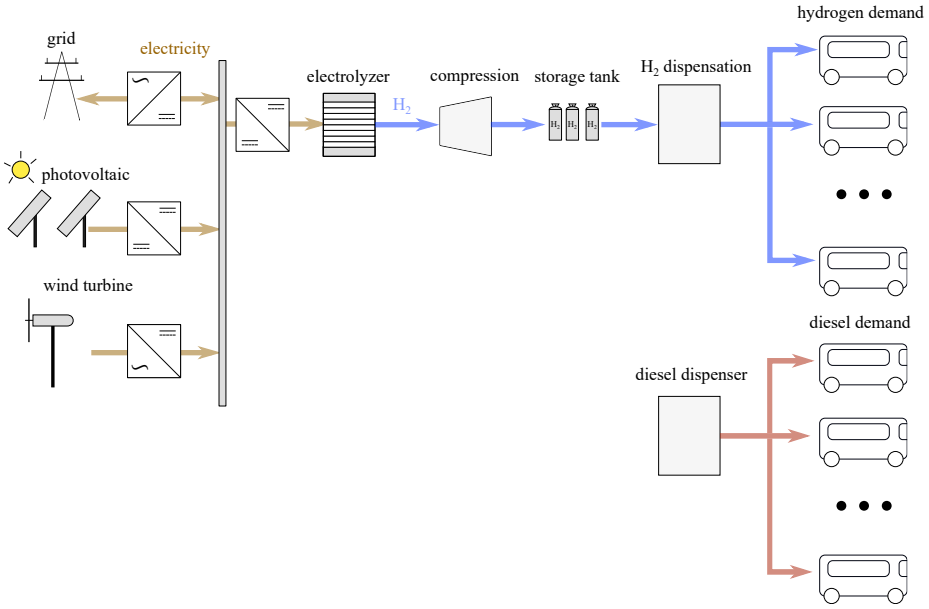


Figure 2: The bus fleet can consist of hydrogen-powered buses, diesel-powered buses or a mix of both. For the hydrogen-powered buses, a grid-connected hydrogen refueling station is considered. In the hydrogen refueling station, a photovoltaic array and wind turbine array produce electricity to generate hydrogen in the electrolyzer. The produced hydrogen is compressed and stored in storage tanks, before dispensation.

pressor, grid electricity is extracted to cover the remaining demand. The grid is considered permanently available, which means that the electricity demand to cover the hydrogen demand is always complied with (by the wind turbines, PV array and/or the grid). Alternatively, when the storage tank is able to comply with the instantaneous hydrogen demand, the PV electricity and wind electricity are used to produce and compress hydrogen. No grid reinjection is considered, as it remains highly uncertain how the grid tariff methodology will adapt after the current integration of digital meters, which ends the current net metering regime [49]. Therefore, this approach mitigates the risk of changing metering regimes, it provides globally applicable conclusions and it illustrates the raw potential of local renewable energy storage.

### *2.2. Component models*

To develop the HRS model, separate models are adopted for each component, and combined in a Python script which contains the power management strategy and quantifies the quantities of interest.

#### *2.2.1. Photovoltaic array*

To determine the electricity produced by a PV array, we imported the model from the *PVlib* Python library [50], which has been validated with experimental data and commercial software [51]. The model quantifies the PV panel power production through a current-voltage characteristic:

$$I_{\mathrm{PV}} = I_{\mathrm{L}} - I_0 \left( \exp\left( \frac{U + IR_{\mathrm{s}}}{n_{\mathrm{diode}} N_{\mathrm{s}} U_{\mathrm{th}}} \right) - 1 \right) - \frac{U + IR_{\mathrm{s}}}{R_{\mathrm{sh}}}, \tag{1}$$

for which the parameters are derived from manufacturer data. Additional information on the parameters and the PV model is present in the Supporting Information. The PV current depends, among others, on solar irradiance and ambient temperature. We adopted the Typical Meteorological Year data for the hourly solar irradiance and ambient temperature from a method we used successfully before [52]. To illustrate the resulting power produced by the PV array, the hourly capacity factor (averaged per month) is presented in Figure 3.

#### *2.2.2. Wind turbine*

We adopted the hourly wind power profile from renewables.ninja, a framework where wind turbine models and power output data are based on the work of Staffell et al. [53]. This framework provides enhanced wind power profiles by the reanalysis of past weather data. Furthermore, this data is corrected with a bias factor to obtain realistic power data via a virtual wind farm model for any location in Europe with a high spatial and temporal accuracy. Additional information on the wind turbine model is present in the Supporting Information. We based the hourly capacity factor profile of a wind turbine model (Enercon E70/2000), which was integrated into the framework of Staffell et al. [53]. This

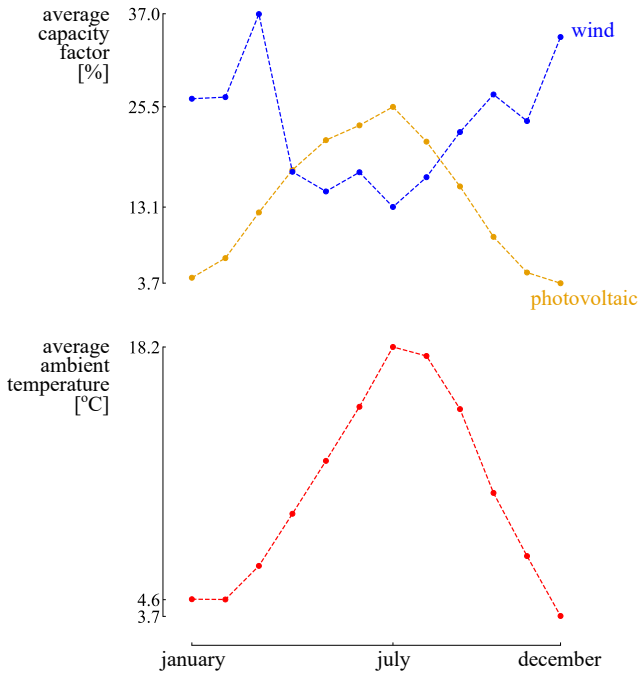


Figure 3: For Brussels (Belgium), the monthly average capacity factor for the photovoltaic array and the monthly average ambient temperature show a similar pattern. However, the wind turbine capacity factor is opposite to the monthly average ambient temperature and monthly average photovoltaic capacity factor.

turbine model and location in Brussels provided an annual mean wind capacity factor of 23.1%, which corresponds to the average wind capacity factor of Belgium for onshore wind turbine farms [53, 54]. Generally, the average monthly wind capacity factor shows a higher capacity factor for wind than for PV at the same location, with a dip between May and August (Figure 3).

### *2.2.3. Electrolyzer*

To convert water into hydrogen by using electricity, we adopted the PEM electrolyzer technology. A PEM electrolyzer promises a fast response time (<1 s) and full operational flexibility, which are significant benefits when coupled to an intermittent energy supply [48]. To model the electrolyzer hydrogen production and corresponding energy consumption, we adopted the model from Abdin et al. [55], which has been validated with experimental current-voltage

curves from Marangio et al. [56]. From this model, the produced hydrogen molar flow rate $\dot{n}_{H_2}$ is quantified depending on the applied current $I_{PEM}$:

$$\dot{n}_{H_2} = \frac{I_{PEM}}{2F}. \tag{2}$$

To determine the current from the applied power, the operating voltage that corresponds to the current needs to be quantified. The operating voltage is characterized according to the following equation:

$$U_{PEM} = U_{oc} - U_{act} - U_{ohm} - U_{con}, \tag{3}$$

where the open-circuit voltage $U_{oc}$, activation overpotential $U_{act}$, ohmic overpotential $U_{ohm}$ and concentration overpotential $U_{con}$ depend, among others, on the operating temperature, pressure and current. Additional information on the quantification of these overpotentials can be found in the Supporting Information.

*2.2.4. Compressor*

A compressor pressurizes the produced hydrogen gas from the electrolyzer array up to the required pressure in the hydrogen storage tank. The hydrogen storage tank requires a pressure of 440 bar to create an overpressure when fueling the FCEB according to the National Institute of Standards [57]. We considered an isentropic compression process to calculate the necessary power for storing the hydrogen gas in the tank at 440 bar with the following equation:

$$P_{compressor} = \frac{\dot{m}_{H_2}}{\eta_c} \frac{k}{k-1} R_{H_2} T_{in} \left[ \left( \frac{p_{out}}{p_{in}} \right)^{\left(\frac{k-1}{k}\right)} - 1 \right], \tag{4}$$

where $\dot{m}_{H_2}$ is the mass flow rate, $\eta_c$ is the compressor efficiency (85%), $k$ is the ratio of specific heats (1.4), $R_{H_2}$ the gas constant of hydrogen (4.12 kJ/kgK), $T_{in}$ is the inlet temperature (353 K) and $p_{in}/p_{out}$ is the inlet/outlet pressure (20 bar and 440 bar, respectively). These parameters provide a specific compression energy of 2.36 $kWh/kg_{H_2}$, which remains in the range of the real energy consumption of compressors in HRS (in reality, such installation requires a specific compression energy between 2 $kWh/kg_{H_2}$ and 4 $kWh/kg_{H_2}$ [57]).

*2.3. Quantities of interest*

To evaluate the system performance, an economic and environmental quantity of interest are defined for this system. For the economic quantity of interest, the Levelized Cost Of Driving (LCOD) is selected, which corresponds to the annualized system cost per unit of distance covered by the bus fleet $D$:

$$\mathrm{LCOD} = \frac{\mathrm{CAPEX_a} + \mathrm{OPEX_a} + C_{\mathrm{repl,a}} + C_{\mathrm{grid,a}} + C_{\mathrm{diesel,a}}}{D}. \tag{5}$$

The annualized capital expense of the system $\mathrm{CAPEX_a}$ corresponds to the sum of the capital expenses for each component, scaled by the Capital Recovery Factor (CRF) [58]:

$$\mathrm{CAPEX_a} = \mathrm{CRF} \sum_{k=0}^{c} N_k \mathrm{CAPEX}_k, \tag{6}$$

where $c$ is the list of different components (i.e., PV array, wind turbine array, PEM electrolyzer array, compressor, storage tank, dispenser, DC-DC converters, AC-DC inverter, FCEB and diesel buses) and $N$ corresponds to the installed capacity. The CRF is determined by the real interest rate $i$ and the system lifetime $L$ (20 years):

$$\mathrm{CRF} = \frac{i(1+i)^L}{(1+i)^L - 1}, \tag{7}$$

where the real interest rate $i$ considers the effect of inflation $f$ on the nominal interest rate $i'$:

$$i = \frac{i' - f}{1+f}. \tag{8}$$

The annualized operating expenses $\mathrm{OPEX_a}$ are defined in a similar matter [58]:

$$\mathrm{OPEX_a} = \sum_{k=0}^{c} N_k \mathrm{OPEX}_k. \tag{9}$$

The annualized replacement cost considers the costs related to the replacement of components during the system lifetime [58]:

$$C_{\mathrm{repl,a}} = \mathrm{CRF} \sum_{k=0}^{c} \left( N_k R_{\mathrm{c,k}} \sum_{l=0}^{r_k} (1+i)^{-l t_k} \right), \tag{10}$$

where $r_k$ is the number of replacements during the system lifetime for every component and $t_k$ is the replacement period. In addition to the component costs, the price for the annual grid electricity bought $C_{\mathrm{grid,a}}$ and for the annual diesel bought $C_{\mathrm{diesel,a}}$ is considered in the total cost. The wholesale electricity price corresponds to 40 % of the total electricity price for buying electricity, while the remaining 60 % depends on transmission cost, distribution cost, taxes and surcharges.

Similar to the LCOD, the environmental quantity of interest represents the annualized GHG emission of the system per unit of distance travelled by the bus fleet (i.e., the Carbon Intensity (CI)):

$$\mathrm{CI} = \frac{\mathrm{GHG}_{\mathrm{comp,a}} + \mathrm{GHG}_{\mathrm{grid,a}} + \mathrm{GHG}_{\mathrm{diesel,a}}}{D}. \tag{11}$$

The system GHG emissions represent the sum of the annualized GHG emissions during construction of the components $\mathrm{GHG}_{\mathrm{comp,a}}$, the GHG emissions from grid electricity consumption $\mathrm{GHG}_{\mathrm{grid,a}}$ and the well-to-wheel GHG emissions from diesel consumption $\mathrm{GHG}_{\mathrm{diesel,a}}$. These parameters are quantified similarly to the annualized capital expenses, grid electricity cost and diesel cost, respectively. Hence, the CI quantifies the total GHG emissions, related to the entire system over the lifetime, including the emissions during the construction of the buses and the components in the renewable-powered hydrogen refueling station. Note that, in this work, the assessment of resource depletion (e.g., water consumption during electrolysis) and the emissions related to recycling of the components is not considered. The adopted values for the specific costs and GHG emissions are presented in Appendix (Table A.3 and Table A.4).

### *2.4. Robust design optimization*

In the adopted formulation of surrogate-assisted RDO, the objective is to minimize the mean and standard deviation for the LCOD and CI [45]. Hence, the strategy aims to simultaneously minimize the average performance of the system (i.e., minimizing the mean) and the sensitivity to the random environment in a quantity of interest (i.e., minimizing the standard deviation). The

sensitivity of a proposed design to the random environment for a specific quantity of interest (i.e., the standard deviation for the LCOD or CI) is reduced by optimizing the design variables, as opposed to reducing the uncertainties from the random environment.

The design space is characterized by five continuous design variables (Table 2). The design variables are the capacity of the components, i.e., the capacity of the PV array, wind turbine array, electrolyzer array and storage tank. In addition, the fraction of the bus fleet fueled by hydrogen is a design variable as well. In other words, the optimizer can decide on the number of FCEB in the bus fleet, while the remaining part is covered by diesel buses. Moreover, as the design variables are considered independent, the optimization algorithm can exclude a technology from the HRS by setting its capacity equal to zero (i.e., the lower bounds of the design variables related to the components). To avoid unreasonable designs and to avoid that the computational budget is spent on evaluating designs with unreasonably large capacities, the design variable upper bounds are selected based on the expected order of magnitude for the optimized designs.

Table 2: The design variables are the capacity of the components in the renewable-powered hydrogen refueling station and the fraction of the bus fleet covered by Fuel Cell Electric Buses.

| design variable | lower bound | upper bound | unit |
|---:|:---:|:---:|:---|
| photovoltaic array | 0 | 10 | $MW_p$ |
| wind turbine array | 0 | 20 | MW |
| PEM electrolyzer array | 0 | 10 | MW |
| hydrogen storage | 0 | 500 | MWh |
| fraction bus fleet on hydrogen | 0 | 100 | % |

The techno-economic and environmental uncertainties are defined by distribution parameters (Subsection 2.4.1). The propagation of these distributions through the system model and the quantification of the corresponding mean and standard deviation of the LCOD or CI is performed using sparse PCE

(Subsection 2.4.2). These statistical moments are used as objectives during the RDO procedure. To find the optimized designs samples, a metaheuristic optimization algorithm is selected (Subsection 2.4.3). During the optimization procedure, a sparse PCE is constructed for each design sample, to determine the corresponding fitness values (i.e., the mean and standard deviation of the quantity of interest) for each design sample. This RDO procedure is elaborated in Subsection 2.4.4.

### *2.4.1. Model inputs: Uncertainty characterization*

In this work, technical, economic, and environmental parameters are subject to uncertainty. As only a handful of data points exist for these parameters, determining the underlying distribution is not feasible. Therefore, we assumed a Uniform distribution for all uncertainties, specified by a lower bound and upper bound value (Table A.3 and Table A.4). The parameters are divided into two categories: Parameters subject to aleatory uncertainty (Table A.3) and parameters subject to epistemic uncertainty (Table A.4). The epistemic uncertainty symbolizes the lack of knowledge on the value of a parameter. This lack of knowledge can be addressed by gaining more information (e.g., defining the actual compressor used and adopting its specific performance parameters as opposed to implementing a generic compressor model with typical parameter values). The aleatory uncertainty represents the natural variation of the parameter and is therefore irreducible (e.g., the evolution of the diesel price in the coming years remains uncertain, independent from the number of predictions available).

The parameters subject to an aleatory uncertainty are the grid electricity price, grid electricity GHG emissions, diesel price, energy consumption, annual solar irradiance, average ambient temperature and the inflation rate (Table A.3). These parameters continuously change during the lifetime of the system and are therefore driven by changes in the future, outside the control of the system designer. The uncertainty on the evolution of the grid electricity price is adopted from 6 prediction scenarios [59]. Similar for the evolution of the diesel price up

to 2040, where the distribution integrates over low, middle and high diesel cost scenarios [60]. The uncertainty on the energy consumption of the hydrogen-powered and diesel-powered buses is adopted from the quantified difference between predicted and real-world operating conditions for these buses [61]. The uncertainty on the specific GHG emission for grid electricity consumption depends on the scenarios for the evolution of the electricity mix up to 2040 [62]. The solar irradiance and ambient temperature are characterized by a Typical Meteorological Year for which the uncertainty is characterized based on the interannual variability [63]. The annual average capacity factor for the wind turbine array is based on hourly data between 1980 and 2020 for Belgium [53].

For each component, the economic and environmental parameters are subject to epistemic uncertainty (Table A.4). Indeed, by considering generic models, the uncertainty lies in the lack of specifying the exact characteristics of the component. To illustrate, the CAPEX for each component is subject to the current price range on the market. As the investment cost is paid at the beginning of the project, no future (i.e., aleatory) uncertainty is considered for this parameter. Similar assumptions are made on the GHG emissions during the manufacturing of each component. To illustrate, the uncertainty on the GHG emissions during the manufacturing of the hydrogen storage tank relates to the amount of recycled steel that has been used, an uncertainty that can be addressed by specifying the hydrogen tank and its manufacturer.

#### *2.4.2. Inner loop: Uncertainty quantification*

As the RDO strategy aims to minimize the mean and standard deviation for a quantity of interest, a UQ algorithm is required to quantify the statistical moments on the quantity of interest, for each design considered during the optimization procedure. We adopted a sparse PCE method, which is a computationally-efficient method to perform UQ on a system with a large stochastic dimension (i.e., $> 15$ uncertain parameters) [44]. In brief, a PCE representation for the input-output relation of the system model consists of a

set of orthogonal polynomials $\Psi$, characterized by coefficients $u$:

$$\hat{M}(\boldsymbol{\xi}) = \sum_i u_i \Psi_i(\boldsymbol{\xi}) \approx M(\boldsymbol{\xi}), \tag{12}$$

where $\boldsymbol{\xi} = (\xi_1, \xi_2, ..., \xi_d)$ is a vector for the independent random parameters and $d$ is the stochastic dimension. In a conventional PCE, the number of orthogonal polynomials (and thus coefficients) in the PCE is defined as follows:

$$P + 1 = \frac{(p+d)!}{p!d!}, \tag{13}$$

where $p$ corresponds to the maximum total order of the orthogonal polynomials. While in conventional PCE, $P + 1$ orthogonal polynomials are added to the expansion and at least $2(P + 1)$ training samples are required to find the corresponding coefficients through regression [40], the adopted sparse PCE includes only the most significant coefficients (and corresponding polynomials) in the truncated series [44]. To determine these significant coefficients a priori, the algorithm starts with an initial set of training samples. Based on the output of these training samples, $P + 1$ one-predictor surrogate models are created and assessed individually by comparing their response to the training samples with the actual model response. The best one-predictor model delivers the first coefficient to the final regression model. This process is repeated on the remaining one-predictor models (i.e., without the previous best one-predictor model) until the maximum number of iterations is reached. Additional details on this sparse PCE method are described by Abraham et al. [44].

The sparse PCE algorithm should be characterized in such a way that, for each design configured during the RDO, accurate statistical moments are provided for each quantity of interest. The two main parameters for the characterization of the sparse PCE are the maximum total order $p$ and the number of training samples. The characterization of these two parameters is performed based on a screening method [45]. First, a set of design samples (i.e., samples with values for the five design variables) is created using Latin Hypercube Sampling, to ensure optimized coverage of the design space. For each design

sample, the Leave-One-Out error [40] is evaluated for a conventional full PCE with different polynomial order. The worst Leave-One-Out error among the design samples is compared with a threshold value. A polynomial order of 2 results in a worst-case Leave-One-Out error below 1% for both quantities of interest (i.e., LCOD and CI). For this polynomial order, which determines the number of orthonormal polynomials available to construct the sparse PCE, the number of training samples needs to be defined. For each design sample, a set of sparse PCEs are created, with an increasing number of initial training samples (Figure 4). For each sparse PCE, the mean and standard deviation are compared with the statistical moments retrieved by Monte Carlo Simulation ($10^4$ samples). Similar to the determination of the polynomial order, the design sample with the highest amount of training samples needed to achieve a converged sparse PCE determines the number of training samples adopted for each design sample during RDO. For the LCOD and CI, 25 % and 48 % of the training samples are needed to ensure an error below $\pm 1$ %, respectively, when compared to a conventional PCE.

*2.4.3. Outer loop: Design optimization*

To optimize the statistical moments, the Nondominated Sorting Genetic Algorithm (NSGA-II) is adopted [64]. The algorithm is extensively used in RDO [65] and because no information is needed on the derivative of the input-output relation, NSGA-II is suitable for complex and highly non-linear models [42, 66]. NSGA-II is a gradient-free, population-based optimizer that uses heuristics to converge to an optimized solution. Starting from an initial population that contains a set of design samples, offsprings are created using a binary tournament selection, crossover and mutation rules. Out of the population and offsprings, the design samples for the new population are selected based on non-dominated sorting. Out of this new population, offsprings are again created and the procedure is repeated until the termination criterion is reached. Additional details on NSGA-II are provided by Deb et al. [64].

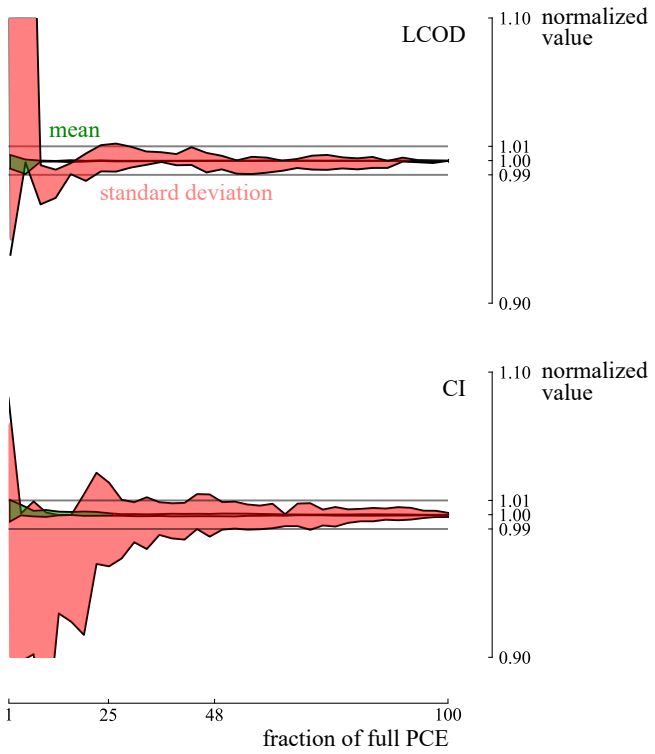


Figure 4: Based on the design sample with the worst convergence, the sparse PCE reaches statistical moments with an error below ±1 % on the Levelized Cost Of Driving (LCOD) and Carbon Intensity (CI) at 25 % and 48 % of the training samples needed for a conventional Polynomial Chaos Expansion (PCE), respectively.

### *2.4.4. Main procedure*

The surrogate-assisted RDO algorithm consists of NSGA-II to perform the optimization, which iteratively generates design samples and evaluates their performance in the fitness values (i.e., mean and standard deviation of the LCOD and CI). Sparse PCE is applied on each design sample to provide the statistical moments as fitness values for the optimization. The first step consists of generating a first population of design samples via Latin Hypercube Sampling [67]. For each design sample in this first population, a PCE is constructed for each quantity of interest. Note that only one set of training samples is required to generate all the required PCEs for a design sample, as each sample generates a value for each quantity of interest. Out of the initial population, an offspring

is created, for which the same procedure is applied: a PCE is created for each quantity of interest and the corresponding mean and standard deviation are stored as fitness values. When the mean and standard deviation values are quantified for each design sample, the design samples in the population and offspring are combined and ranked based on their dominance in the objectives (i.e., non-dominated sorting). The top half of the design samples lead to the next generation of design samples. Out of this new generation, offsprings are again created and the new population and offspring are again ranked, leading to the next generation. This process is repeated until the computational budget is spent.

## 3. Results and discussion

The results are provided in two parts. In the first part, RDO is performed separately for each quantity of interest (i.e., LCOD and CI). These results illustrate the trade-off between minimizing the mean and standard deviation for each quantity of interest and the design trends between the corresponding optimized designs. In the second part, a holistic RDO is performed, considering the mean and standard deviation of both quantities of interest simultaneously as objectives. This strategy suggests holistic optimized designs, which consider both the stochastic performance in LCOD and CI. Note that none of the optimized designs proposed are constrained by the design variable bounds (Table 2).

### *3.1. Individual Robust Design Optimization*

An RDO is performed for each quantity of interest. The RDO on the LCOD is presented first, followed by the RDO on the CI and an overall performance comparison between the two sets of optimized designs.

#### *3.1.1. Robust Design Optimization of the Levelized Cost Of Driving*

The RDO algorithm considers the LCOD mean and LCOD standard deviation as optimization objectives. The results illustrate a trade-off between minimizing the LCOD mean and minimizing the LCOD standard deviation

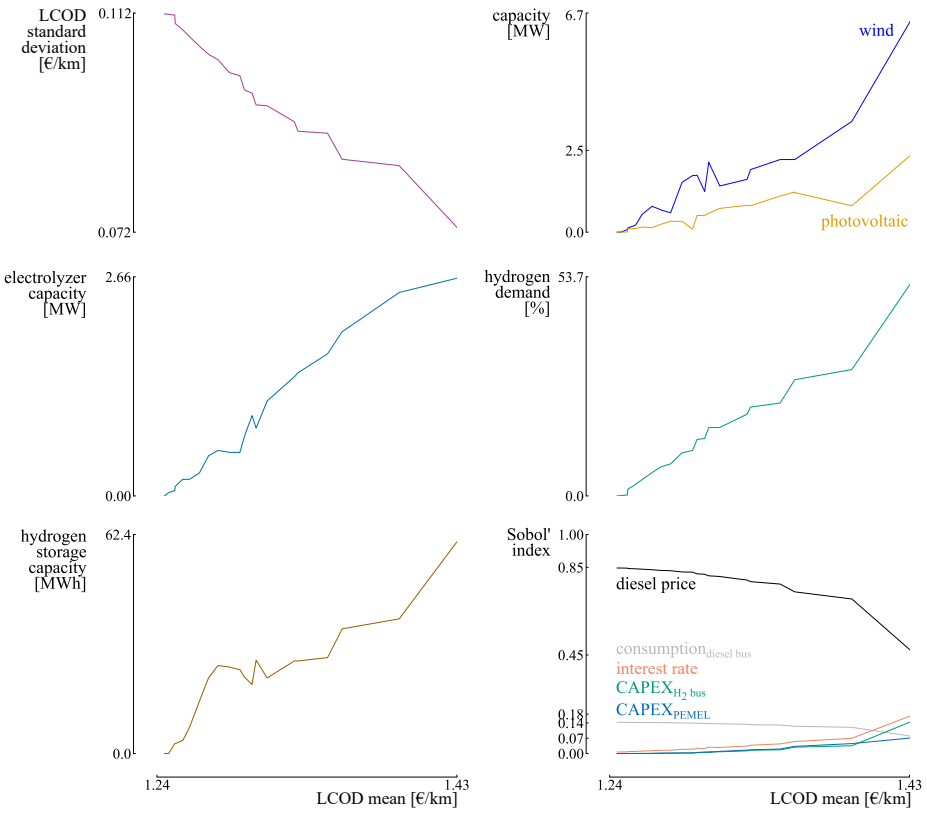


Figure 5: The Pareto front illustrates a trade-off between minimizing the Levelized Cost Of Driving (LCOD) mean and LCOD standard deviation. To achieve the optimized LCOD mean, only diesel-powered buses are considered (i.e., no hydrogen demand). The LCOD standard deviation is reduced by subsequently converting the diesel-powered buses into Fuel Cell Electric Buses (FCEB), accompanied by a Hydrogen Refueling Station with increasing wind power, photovoltaic power and hydrogen storage.

(Figure 5, top-left). Hence, no single design exists for this system, subject to the considered techno-economic and environmental uncertainties, that simultaneously achieves the lowest LCOD mean and lowest LCOD standard deviation. The design with the best mean achieves an LCOD mean of 1.24 €/km, with a standard deviation of 0.11 €/km. Alternatively, the robust design (i.e., with the lowest LCOD standard deviation) decreases the LCOD standard deviation by 36 % (0.07 €/km), at the expense of an increase in LCOD mean by 11 % (1.43 €/km). To achieve the optimized LCOD mean, no FCEB are considered

in the design, resulting in a complete diesel-powered bus fleet (Figure 5, middle-right). Consequently, no hydrogen production is required (Figure 5, middle-left) and thus no renewable capacity is considered (Figure 5, top-right). With only diesel-powered buses, the main drivers of the LCOD standard deviation (Figure 5, bottom-right) are the uncertainty on the future diesel price (Sobol' index: 0.85) and the uncertainty on the actual fuel consumption of the diesel buses (Sobol' index: 0.14).

To achieve a lower LCOD standard deviation than the diesel-powered bus fleet, the optimized designs are subsequently configured with an increasing hydrogen demand, supported by a renewable-powered HRS. Hence, converting a fraction of the diesel-powered bus fleet into FCEB, which are fueled by a renewable-powered HRS, reduces the LCOD standard deviation. The robust design is configured with a 2.5 $MW_p$ PV array, 6.7 MW wind turbine, 2.7 MW electrolyzer array and 62 MWh (90 $m^3$) hydrogen storage tank, covering 54 % of the bus fleet with FCEB. With 500 $kg_{H_2}$/day, the order of magnitude of the design components is similar to the ones of a renewable-powered HRS in Turkey (1.6 MW wind turbine, 300 kW PV array, 600 kW PEM electrolyzer, 30 MWh hydrogen storage tank), which delivers 125 $kg_{H_2}$/day [68]. As 46 % of the bus fleet is still fueled by diesel, the LCOD standard deviation for the robust design remains mainly driven by the uncertainty on the diesel price (Sobol' index: 0.45) and the uncertainty on the diesel consumption (Sobol' index: 0.07), accompanied by a significant share coming from the uncertainty on the interest rate (Sobol' index: 0.18), the CAPEX of the FCEB (Sobol' index: 0.17) and the CAPEX of the electrolyzer array (Sobol' index: 0.07). Interestingly, a higher share of the bus fleet powered by hydrogen ($> 54\%$), accompanied by a larger renewable-powered HRS, leads to a rise in both the LCOD mean and LCOD standard deviation. This can be explained by the rising uncertainty related to the HRS, which overcompensates the reducing contribution of the uncertainty on the diesel price and diesel consumption to the LCOD standard deviation.

*3.1.2. Robust Design Optimization of the Carbon Intensity*

Contrary to the RDO on the LCOD, nearly no trade-off exists between minimizing the CI mean and minimizing the CI standard deviation (Figure 6, top-left). Among the optimized designs, the optimized CI mean ranges only between $0.154\,\mathrm{kg_{CO_2,eq}}$/km and $0.160\,\mathrm{kg_{CO_2,eq}}$/km, to achieve a small reduction in CI standard deviation from $0.0156\,\mathrm{kg_{CO_2,eq}}$/km to $0.0134\,\mathrm{kg_{CO_2,eq}}$/km. All optimized designs consider a bus fleet entirely consisting out of FCEB, i.e., no diesel-powered buses are present in the bus fleet. As the electrolyzer capacity is typically scaled with the hydrogen demand, the electrolyzer array capacity is similar for all optimized designs (6.8 MW). The optimized CI mean is achieved by solely considering a wind turbine array (15.7 MW), while the robust design consists of a slightly smaller wind turbine array (14.1 MW), supported by a PV array of $1\,\mathrm{MW_p}$ (Figure 6, top-right). Following the reduced wind array capacity and the increased PV array capacity in the robust design, the match between the renewable power production profile and the hydrogen demand profile (during the evening, night and early-morning) is worse. To store the additional hydrogen produced outside the dispensation hours, the hydrogen storage capacity is increased up to 203 MWh in the robust design (Figure 6, bottom-left). The Sobol' indices for the optimized CI mean design illustrate that the uncertainty on the GHG emissions related to the wind turbine array construction (Sobol' index: 0.76) and the uncertainty on the wind capacity factor (Sobol' index: 0.14) are the main drivers of the CI standard deviation (Figure 6, bottom-right). Furthermore, the CI for this design is significantly affected by the actual wind capacity factor, which means that the hydrogen storage tank does not cover the load during the entire year. Instead, part of the hydrogen demand is covered by the actual wind power available, which is sensitive to the wind capacity factor. By gradually increasing the hydrogen storage and replacing a fraction of the wind turbine array with a PV array, the robust design removes the contribution of the uncertainty on the wind capacity factor to the CI standard deviation by relying on the stored hydrogen, filled outside dispensation hours, to cover

the hydrogen demand. Instead, the uncertainty related to the GHG emissions during construction of the hydrogen storage tank (Sobol' index: 0.10) and PV array (Sobol' index: 0.06) gain importance.

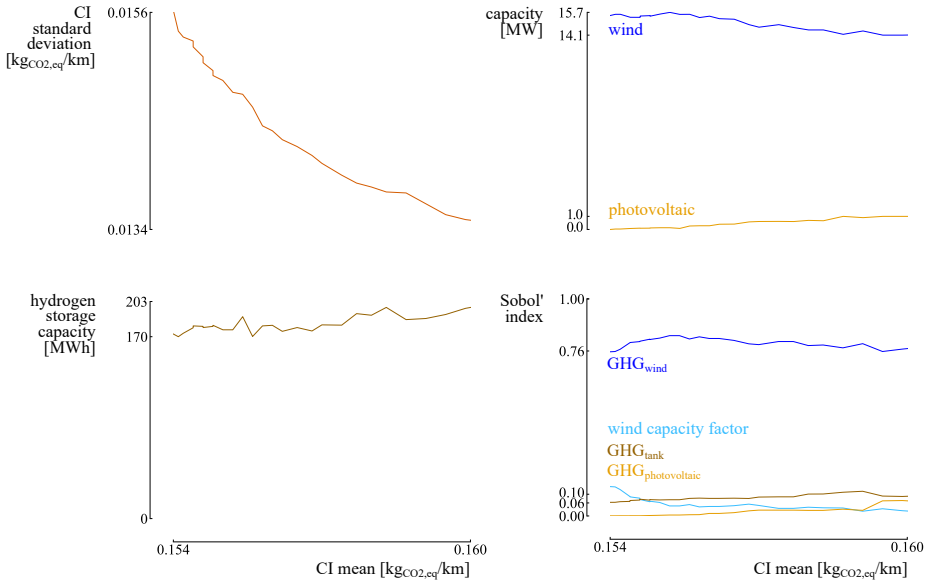


Figure 6: The Pareto front illustrates a trade-off between minimizing the Carbon Intensity (CI) mean and CI standard deviation. Considering only wind power results in the optimized CI mean, while the robust CI is achieved by removing the dependency on the wind capacity factor uncertainty, through replacing part of the wind capacity with photovoltaic capacity and increasing the hydrogen storage capacity.

### *3.1.3. Overall performance comparison*

As illustrated in the RDO results on each individual quantity of interest, the optimized stochastic designs for the CI and LCOD clearly differ in design characteristics. Therefore, the performance from the optimized designs in one quantity of interest might result in a poor performance in the other quantity of interest. Indeed, when comparing the performance in CI for the designs optimized in LCOD (and the other way around), the performance is significantly worse (Figure 7).

As expected from the RDO on the CI, the relatively small trade-off between minimizing the CI mean and minimizing the CI standard deviation results in a

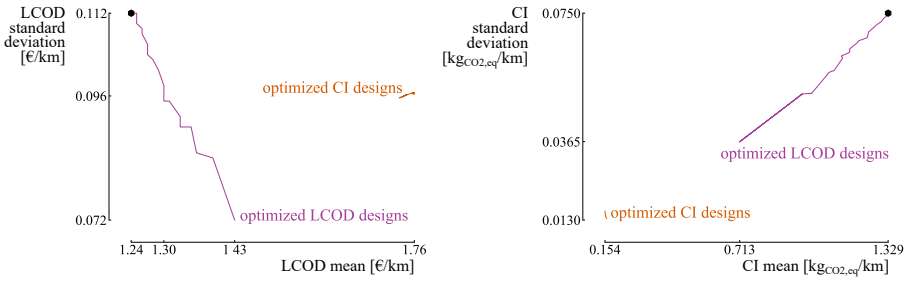


Figure 7: The performance in one quantity of interest of the designs optimized for the other quantity of interest illustrates a clear trade-off between optimizing the stochastic performance for the two quantities of interest.

small range on the LCOD performance for these designs (Figure 7, optimized CI designs). The optimized CI designs achieve an acceptable LCOD standard deviation, around 0.096 €/km, which ranges between the minimum and maximum LCOD standard deviation achieved by the optimized LCOD designs. However, the optimized CI designs achieve a significantly higher LCOD mean. To illustrate, when comparing with the optimized LCOD mean design that achieves a similar LCOD standard deviation of 0.096 €/km, the LCOD mean for the optimized CI design is 35 % higher (i.e., LCOD mean of 1.76 €/km, as opposed to 1.30 €/km).

Among the optimized designs, all optimized LCOD designs perform worse in both CI mean and CI standard deviation (Figure 7, optimized LCOD designs). The worst-performing optimized LCOD design achieves a CI mean of 1.33 $\mathrm{kg_{CO_2,eq}}$/km, with a CI standard deviation of 0.075 $\mathrm{kg_{CO_2,eq}}$/km. This design corresponds to the design with the optimized LCOD mean of 1.24 €/km and is characterized by a complete diesel-powered fleet. This comparison shows that, when considering an optimized LCOD design with a reduced LCOD standard deviation, this design also improves both the CI mean and CI standard deviation.

### *3.2. Holistic Robust Design Optimization*

In the holistic RDO, four objectives are minimized simultaneously (i.e., minimizing the mean and standard deviation for the LCOD and CI). Hence, four

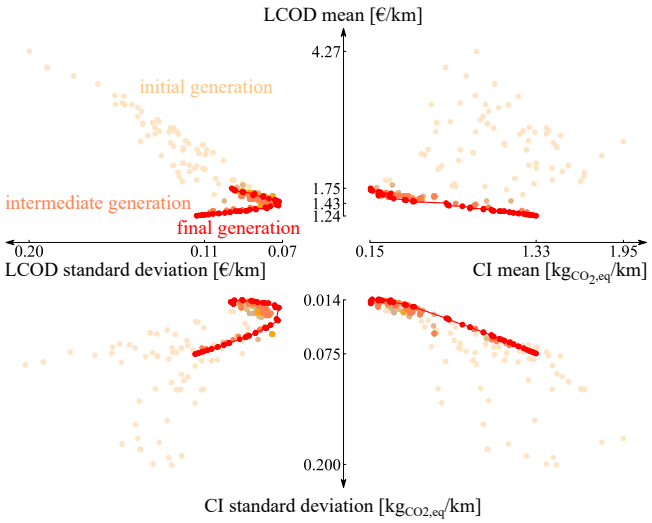


Figure 8: In the holistic Robust Design Optimization (RDO), four objectives are minimized simultaneously (mean and standard deviation for the Levelized Cost of Driving (LCOD) and Carbon Intensity (CI)), in each consecutive generation of design samples. As minimization is desired, the samples converge towards the centre of the cross-plot.

objective values are quantified for each design in a generation of design samples. In each consecutive generation, the design samples converge towards the Pareto set of optimized samples in the final generation (Figure 8). Following the nondominated sorting principle of NSGA-II, a design remains in the Pareto set of optimized designs as long as it dominates every other design in at least one of the four objectives. Consequently, the optimized designs found in the individual RDO (Figure 7) are extended in the holistic RDO (Figure 9).

To illustrate the performance for each design and why each design is considered optimized in the holistic RDO, the achieved LCOD standard deviation, CI mean and CI standard deviation are presented in function of the achieved LCOD mean (Figure 10, left). For the optimized LCOD mean design (1.24 €/km), the worst LCOD standard deviation (0.11 €/km), CI mean (1.33 $\mathrm{kg_{CO_2,eq}}$/km) and CI standard deviation (0.075 $\mathrm{kg_{CO_2,eq}}$/km) are achieved among the optimized designs. Accepting an increase in LCOD mean up to 1.43 €/km results in alternative designs with a reduced CI mean down to 0.71 $\mathrm{kg_{CO_2,eq}}$/km (46 %), re-

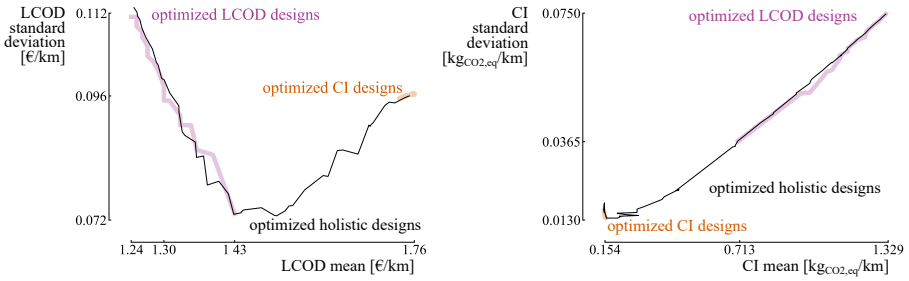


Figure 9: The optimized designs resulting from a Robust Design Optimization (RDO) on each quantity of interest separately reappear in the optimized designs resulting from the holistic RDO (Optimized 4D designs).

duced CI standard deviation down to 0.037 $\mathrm{kg_{CO_2,eq}}$/km (51 %) and a reduced LCOD standard deviation down to 0.07 €/km (37 %), i.e., the robust LCOD (Figure 10, point A). In conclusion, this first subset of designs illustrates that switching from a diesel-powered bus fleet (i.e., the optimized LCOD mean design) into a mobility demand that is partly covered by FCEB (54 %) improves not only the LCOD robustness, but also the average expected CI and the CI robustness.

In the second part of the optimized designs, with an LCOD mean between 1.43 €/km and 1.62 €/km, the LCOD standard deviation is increasing, as the robust LCOD design was reached at an LCOD mean of 1.43 €/km. Hence, this subset of optimized designs is not considered Pareto-optimal in the LCOD statistical moments. Instead, accepting alternative designs with an increase in LCOD mean up to 1.62 €/km results in a continuous decrease in CI mean and CI standard deviation (Figure 10, point B). In these designs, the fraction of the mobility demand converted into FCEB is increased up to 96 % (Figure 10, middle-right), accompanied by an increase in the size of the wind turbine array (Figure 10, top-right) and the hydrogen storage tank (Figure 10, bottom-right). Due to the significant mean and significant uncertainty on the GHG emissions during construction of the PV array, the optimizer does not further increase the capacity of the PV array in this subset of optimized designs. Thus, this second subset of optimized designs provides intermediate solutions between the

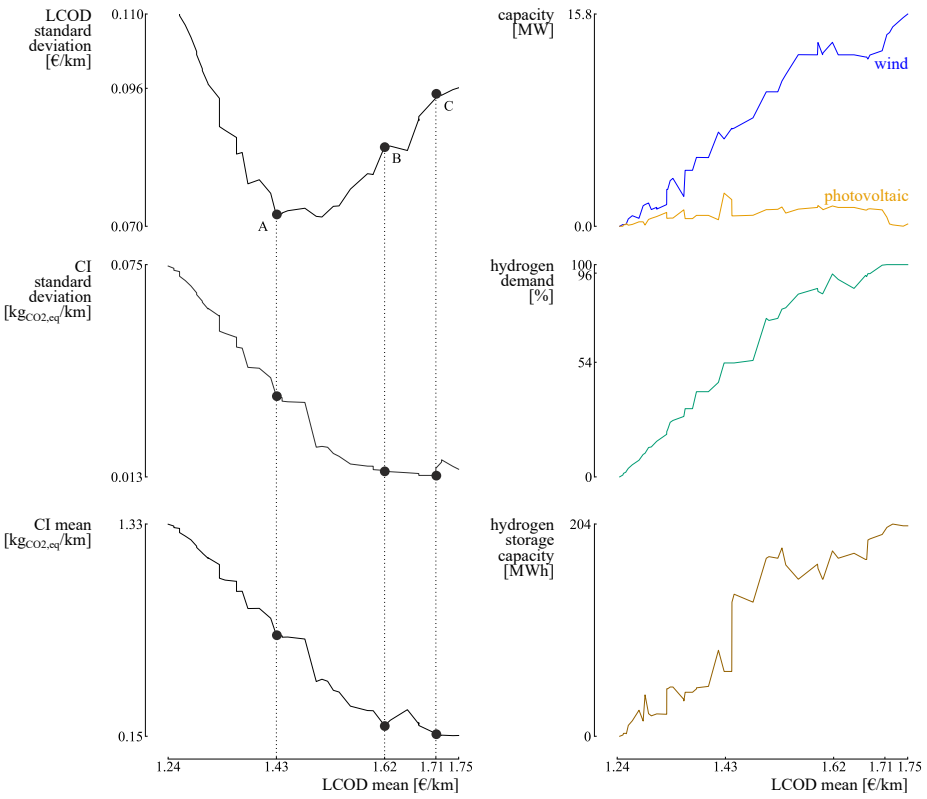


Figure 10: The results from the holistic Robust Design Optimization (RDO) illustrate that the optimized Levelized Cost Of Driving (LCOD) mean corresponds to the worst LCOD standard deviation, Carbon Intensity (CI) mean and CI standard deviation. The LCOD standard deviation, CI mean and CI standard deviation are subsequently reduced by gradually replacing the diesel-powered buses with Fuel Cell Electric Buses (FCEB), accompanied by a wind turbine array and photovoltaic array that are scaled accordingly.

stochastic performance of LCOD and CI.

In the third subset of optimized designs, between 1.62 €/km and 1.71 €/km, the robust CI design is reached by converting the remaining diesel-powered buses into FCEB. However, the gain in CI standard deviation is marginal (0.013 $kg_{CO_2,eq}$/km, as opposed to 0.015 $kg_{CO_2,eq}$/km), while the mean CI stabilizes around 0.21 $kg_{CO_2,eq}$/km and the LCOD mean and LCOD standard deviation further increase up to 1.71 €/km and 0.094 €/km, respectively (Figure 10, point C).

The fourth and final subset of optimized designs, with an LCOD mean between 1.71 €/km and 1.75 €/km, reach the optimized CI mean by replacing the PV capacity with an adequate wind power capacity. This final subset corresponds to the optimized designs from the individual RDO on the CI and range between the optimized CI mean (0.15 $kg_{CO_2,eq}$/km) and optimized CI standard deviation (0.013 $kg_{CO_2,eq}$/km) achieved in the holistic RDO.

In addition to modifying the design, the standard deviation on the quantity of objectives can be reduced by reducing the epistemic uncertainty on the input parameters. As indicated on Figure 10, the diesel-powered bus fleet with the optimized LCOD mean of 1.24 €/km results in the worst LCOD standard deviation and worst CI standard deviation among the optimized designs. For this design, the uncertainty on the diesel cost is the main driver for the LCOD standard deviation, while the uncertainty on the consumption of the diesel bus is the main driver for the CI standard deviation (Figure 11). These are aleatory

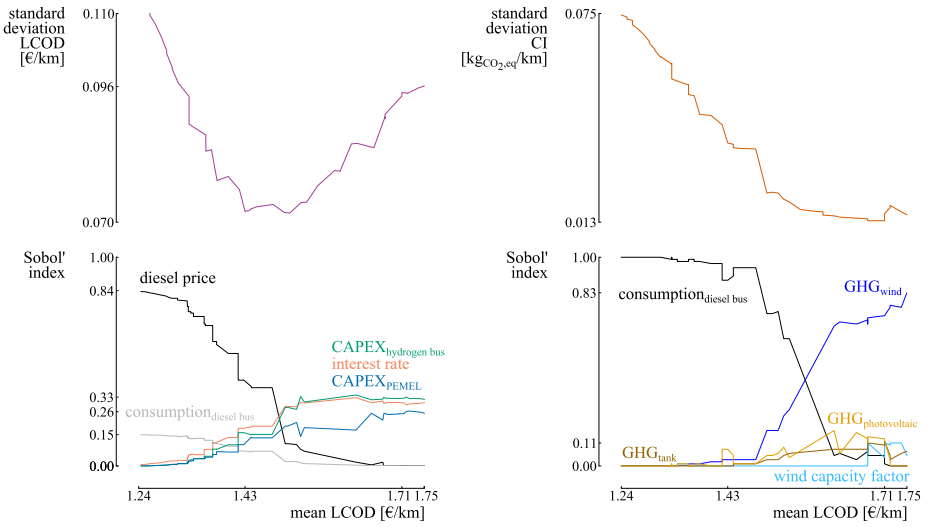


Figure 11: The Sobol' indices on the Levelized Cost Of Driving (LCOD, bottom-left) and the Carbon Intensity (CI, bottom-right) indicate that the design corresponding to the best LCOD mean is subject to the diesel-related aleatory uncertainties, while the designs with higher LCOD mean, between 1.43 €/km and 1.75 €/km, are subject to epistemic uncertainties related to the renewable-powered Hydrogen Refueling Station (HRS).

uncertainties, which means that these uncertainties cannot be reduced by measures taken by the system designer. Up until the robust design for the LCOD, corresponding to an LCOD mean of 1.43 €/km, the LCOD and CI standard deviation are mostly driven by these input uncertainties. However, for the designs for which at least 54 % of the diesel-powered buses are replaced by FCEB (i.e., LCOD mean between 1.43 €/km and 1.75 €/km), the aleatory uncertainties related to diesel-powered buses are replaced by epistemic uncertainties. Hence, the standard deviation of the quantities of interest for the designs which are mainly characterized by FCEB can be reduced by gaining more knowledge on the important uncertainties. To illustrate, for the design corresponding to an LCOD mean of 1.71 €/km (96 % of the bus fleet are FCEB), the main drivers for the LCOD standard deviation are the uncertainty on the CAPEX of the FCEB (Sobol' index: 0.33), interest rate (Sobol' index: 0.32), CAPEX of the electrolyzer array (Sobol' index: 0.26). As the amount of diesel-powered buses in the fleet is negligible, the Sobol' indices corresponding to the diesel price and consumption of the diesel-powered buses are zero. As only epistemic uncertainties remain, the LCOD standard deviation can be reduced by gaining more knowledge on the important parameters. For this design, specifying the PEM electrolyzer and FCEB supplier and determining the finance type are the main actions to reduce the LCOD standard deviation. For the CI standard deviation, the main driver is the uncertainty on the GHG emissions during construction of the wind turbine array. Reducing this uncertainty by specifying the wind turbine technology and manufacturer is the main action to improve the CI robustness.

The LCOD represents the annualized cost of the system (i.e., renewable-powered HRS, FCEB, diesel buses and fuel), per unit of distance covered by the entire bus fleet. As the daily distance covered by the bus fleet is fixed, the annual distance covered by the bus fleet is equal for all the optimized designs. Therefore, the total (annualized) costs and (annualized) GHG emissions can be directly derived from the LCOD and CI, respectively. With an annual distance covered by the bus fleet equal to $3.65 \times 10^6$ km, the annualized cost of the opti-

mized designs ranges between $4.53 \times 10^6$ € and $6.39 \times 10^6$ €, while the annualized GHG emissions ranges between $0.55 \times 10^6$ $\mathrm{kg_{CO_2,eq}}$ and $4.85 \times 10^6$ $\mathrm{kg_{CO_2,eq}}$. Another quantity of interest that is typically adopted for renewable-powered HRS is the Levelized Cost Of Hydrogen (LCOH), corresponding to the annualized cost of the renewable-powered HRS and the FCEB, per kilogram of hydrogen produced by the HRS. For the optimized designs, the LCOH ranges between 17.0 €/$\mathrm{kg_{H_2}}$ and 18.9 €/$\mathrm{kg_{H_2}}$ (Figure 12). The lowest LCOH (17.0 €/$\mathrm{kg_{H_2}}$) among the optimized designs is achieved by the robust design, i.e., the design corresponding to an LCOD mean of 1.43 €/km and LCOD standard deviation of 0.07 €/km. Hence, the lowest LCOH is achieved when 54 % of the bus fleet is covered by FCEB, and the highest LCOH corresponds to a bus fleet fully covered by FCEB, which corresponds to the results reported by Gunawan et al. [7]. Moreover, the LCOH is similar to the ones reported by Gunawan et al. [7] for a renewable-powered HRS for a bus fleet in Ireland (between 11 €/$\mathrm{kg_{H_2}}$ and 22 €/$\mathrm{kg_{H_2}}$).

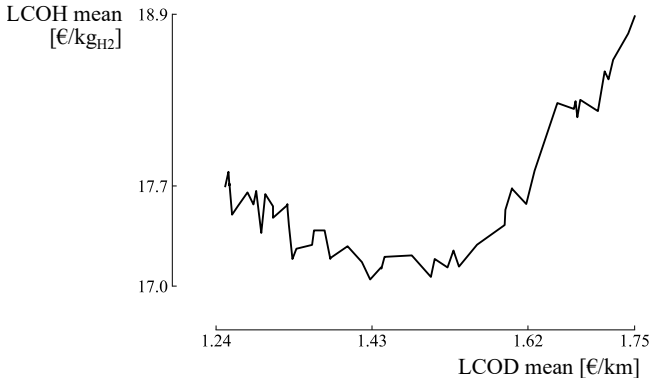


Figure 12: For the optimized designs, the Levelized Cost Of Hydrogen (LCOH) ranges between 17.0 €/$\mathrm{kg_{H_2}}$ and 18.9 €/$\mathrm{kg_{H_2}}$. The robust Levelized Cost Of Driving (LCOD) design, corresponding to an LCOD mean of 1.43 €/km, achieves the lowest LCOH among the optimized designs.

## 4. Conclusion

Renewable-powered Hydrogen Refueling Stations (HRS) for a Fuel Cell Electric Bus (FCEB) fleet achieve an excellent environmental performance, at the expense of a higher fuel cost as opposed to a traditional diesel-powered bus fleet. However, following the significant uncertainties associated with diesel, a renewable-powered HRS might achieve additional benefits in terms of robustness when considering techno-economic and environmental uncertainties.

- A diesel-powered bus fleet achieves the optimized Levelized Cost Of Driving (LCOD) mean of 1.24 €/km, subject to a standard deviation of 0.11 €/km. However, among the optimized designs, a diesel-powered bus fleet achieves the highest Carbon Intensity (CI) mean and CI standard deviation, equal to 1.33 $\mathrm{kg_{CO_2,eq}}$/km and 0.075 $\mathrm{kg_{CO_2,eq}}$/km, respectively.

- The robust design for the LCOD reduces the LCOD standard deviation by 36 % (down to 0.07 €/km), at the expense of an increase in LCOD mean by 11 % (up to 1.43 €/km). This design corresponds to a bus fleet with 54 % FCEB and an HRS consisting of a 6.7 MW wind turbine array, 2.5 MW PV array and 62 MWh hydrogen storage. In addition to the optimized LCOD standard deviation, this design achieves a reduced CI mean of 46 % (0.71 $\mathrm{kg_{CO_2,eq}}$/km) and reduced CI standard deviation of 51 % (0.036 $\mathrm{kg_{CO_2,eq}}$/km) and consequently provides a suitable alternative to a diesel-powered bus fleet.

- The optimized CI mean and optimized CI standard deviation are achieved with a bus fleet entirely consisting out of FCEB. While the optimized CI mean of 0.15 $\mathrm{kg_{CO_2,eq}}$/km is achieved with a wind turbine array of 15.8 MW, the robust alternative for the CI consists of a 14.1 MW wind turbine array and 1.0 MW PV array, enabling to reduce the standard deviation from 0.015 $\mathrm{kg_{CO_2,eq}}$/km to 0.013 $\mathrm{kg_{CO_2,eq}}$/km, at the expense of an increase in CI mean up to 0.16 $\mathrm{kg_{CO_2,eq}}$/km. Nevertheless, these optimized CI designs are subject to a large LCOD mean and LCOD standard

deviation, equal to 1.75 €/km and 0.096 €/km, respectively.

- The robust LCOD design and the optimized CI designs are subject to epistemic (i.e., reducible) uncertainties, while the diesel-powered bus fleet is mainly subject to aleatory (i.e., irreducible) uncertainties. Therefore, the robustness of the renewable-powered HRS can be further improved by reducing the uncertainty on the input parameters.

Future work will focus on the integration of full-electric buses. In addition, to ensure a future-proof installation, the dispensation pressure will be increased up to 700 bar and pre-dispensation cooling will be considered. To cover this additional electricity demand, a battery stack will be included.

## 5. Acknowledgements

The first author acknowledges the support of Fonds de la Recherche Scientifique - FNRS [35484777 FRIA-B2].

## Appendix A. Stochastic data

Table A.3: Parameters affected by aleatory uncertainty.

| parameter | value | unit | Ref. |
|---|---|---|---|
| $\text{consumption}_{\text{diesel bus}}$ | 3.7 - 4.5 | kWh/km | [61] |
| $\text{consumption}_{\text{hydrogen bus}}$ | 3.0 - 3.2 | kWh/km | [61] |
| annual solar irradiance | 1082 - 1266 | $\text{kWh/m}^2$ | [69] |
| annual average wind capacity factor | 20 - 26 | % | [53] |
| average ambient temperature | 9.9 - 10.7 | °C | [69] |
| inflation rate | 1 - 2 | % | [70] |
| wholesale electricity price | 57 - 91 | €/MWh | [59] |
| $\text{GHG}_{\text{electricity}}$ | 144 - 176 | $g_{CO_2,eq}$/kWh | [62] |

| | | | |
|---|---|---|---|
| diesel price | 1.42 - 2.31 | €/l | [60] |

Table A.4: Parameters affected by epistemic uncertainty.

| parameter | value | unit | Ref. |
|---|---|---|---|
| $CAPEX_{PV}$ | 350 - 600 | €/$kW_p$ | [71] |
| $OPEX_{PV}$ | 16 - 19 | €/$kW_p$/year | [72] |
| $GHG_{PV}$ | 520 - 1550 | $kg_{CO_2,eq}$/$kW_p$ | [73] |
| $CAPEX_{wind}$ | 620 - 800 | €/kW | [74] |
| $OPEX_{wind}$ | 18 - 36 | €/kW/year | [74] |
| $GHG_{wind}$ | 242 - 469 | $kg_{CO_2,eq}$/kW | [75] |
| $CAPEX_{PEM}$ | 1400 - 2100 | €/kW | [48] |
| $OPEX_{PEM}$ | 3 - 5 | % of CAPEX | [48] |
| $Repl_{PEM}$ | 15 - 20 | % of CAPEX | [76, 77] |
| $life_{PEM}$ | 60 - 100 | kh | [48] |
| $GHG_{PEM}$ | 190 - 235 | $kg_{CO_2,eq}$/kW | [78] |
| $CAPEX_{tank}$ | 11 - 14 | €/kWh | [79] |
| $OPEX_{tank}$ | 1 - 2 | % of CAPEX | [76, 80] |
| $GHG_{tank}$ | 6 - 12 | $kg_{CO_2,eq}$/kWh | [81] |
| $CAPEX_{compressor}$ | 1000 - 1500 | €/kW | [82] |
| $OPEX_{compressor}$ | 1 - 2 | % of CAPEX | [82] |
| $GHG_{compressor}$ | 80 - 120 | $kg_{CO_2,eq}$/kW | [83] |

| | | | |
|---|---|---|---|
| $CAPEX_{dispenser}$ | 45 000 - 65 000 | €/unit | [7, 19, 79] |
| $OPEX_{dispenser}$ | 1-2 | % of CAPEX | [19] |
| $CAPEX_{diesel\ bus}$ | 220 000 - 250 000 | €/unit | [7, 84, 85] |
| $OPEX_{diesel\ bus}$ | 0.26 - 0.30 | €/km | [85, 86] |
| $GHG_{diesel\ engine}$ | 20.0 - 22.7 | $kg_{CO_2,eq}$/kW | [87, 88] |
| $CAPEX_{hydrogen\ bus}$ | 400 000 - 620 000 | €/unit | [7, 84–86] |
| $OPEX_{hydrogen\ bus}$ | 0.26 - 0.40 | €/km | [7, 85] |
| $GHG_{fuel\ cell}$ | 43 - 61 | $kg_{CO_2,eq}$/kW | [89] |
| $CAPEX_{DC-DC}$ | 40 - 160 | €/kW | [90] |
| $OPEX_{DC-DC}$ | 1 - 5 | % of CAPEX | [90] |
| $CAPEX_{DC-AC}$ | 50 - 200 | €/kW | [90] |
| $OPEX_{DC-AC}$ | 1 - 5 | % of CAPEX | [90] |
| interest rate | 5 - 7 | % | [91–94] |

## References


[1] P. K. Rose, F. Neumann, Hydrogen refueling station networks for heavy-duty vehicles in future power systems, Transportation Research Part D: Transport and Environment 83 (2020) 102358.

[2] C. Wang, Z. Ye, Y. Yu, W. Gong, Estimation of bus emission models for different fuel types of buses under real conditions, Science of the Total Environment 640 (2018) 965–972.

[3] E. R. Grijalva, J. M. López Martínez, Analysis of the Reduction of CO2 Emissions in Urban Environments by Replacing Conventional City Buses by Electric Bus Fleets: Spain Case Study, Energies 12 (3) (2019) 525.

[4] G. Zhang, J. Zhang, T. Xie, A solution to renewable hydrogen economy for fuel cell buses–a case study for zhangjiakou in north china, International journal of hydrogen energy 45 (29) (2020) 14603–14613.

[5] K. G. Logan, J. D. Nelson, A. Hastings, Electric and hydrogen buses: Shifting from conventionally fuelled cars in the UK, Transportation Research Part D: Transport and Environment 85 (2020) 102350.

[6] G. Correa, P. Muñoz, T. Falaguerra, C. Rodriguez, Performance comparison of conventional, hybrid, hydrogen and electric urban buses using well to wheel analysis, Energy 141 (2017) 537–549.

[7] T. A. Gunawan, I. Williamson, D. Raine, R. F. Monaghan, Decarbonising city bus networks in ireland with renewable hydrogen, International Journal of Hydrogen Energy (2020).

[8] R. Fang, Life cycle cost assessment of wind power–hydrogen coupled integrated energy system, International Journal of Hydrogen Energy 44 (56) (2019) 29399–29408.

[9] J. C. Osorio-Aravena, A. Aghahosseini, D. Bogdanov, U. Caldera, N. Ghorbani, T. N. O. Mensah, S. Khalili, E. Muñoz-Cerón, C. Breyer, The impact of renewable energy and sector coupling on the pathway towards a sustainable energy system in Chile, Renewable and Sustainable Energy Reviews 151 (2021) 111557.

[10] F. Contino, S. Moret, G. Limpens, H. Jeanmart, Whole-energy system models: The advisors for the energy transition, Prog. Energy Combust. Sci 81 (2020) 100872.

[11] A. Fattahi, J. Sijm, A. Faaij, A systemic approach to analyze integrated energy system modeling tools: A review of national models, Renewable and Sustainable Energy Reviews 133 (2020) 110195.

[12] S. Collins, J. P. Deane, K. Poncelet, E. Panos, R. C. Pietzcker, E. Delarue, B. P. Ó. Gallachóir, Integrating short term variations of the power system

into integrated energy system models: A methodological review, Renewable and Sustainable Energy Reviews 76 (2017) 839–856.

[13] D. Wang, L. Liu, H. Jia, W. Wang, Y. Zhi, Z. Meng, B. Zhou, Review of key problems related to integrated energy distribution systems, CSEE Journal of Power and Energy Systems 4 (2) (2018) 130–145.

[14] F. Ruiming, Multi-objective optimized operation of integrated energy system with hydrogen storage, International Journal of Hydrogen Energy 44 (56) (2019) 29409–29417.

[15] P. Spath, M. Mann, Life Cycle Assessment of Renewable Hydrogen Production via Wind/Electrolysis: Milestone Completion Report, Tech. rep., National Renewable Energy Lab., Golden, CO.(US) (2004).

[16] J. Burkhardt, A. Patyk, P. Tanguy, C. Retzke, Hydrogen mobility from wind energy–A life cycle assessment focusing on the fuel supply, Applied energy 181 (2016) 54–64.

[17] co2 emissiefactoren, Lijst emissiefactoren, Available online: `https://www.co2emissiefactoren.nl/lijst-emissiefactoren/`. Accessed: 4th February 2021 (2020).

[18] M. Kayfeci, A. Keçebaş, M. Bayat, Hydrogen production, in: Solar Hydrogen Production, Elsevier, 2019, pp. 45–83.

[19] M. Minutillo, A. Perna, A. Forcina, S. Di Micco, E. Jannelli, Analyzing the levelized cost of hydrogen in refueling stations with on-site hydrogen production via water electrolysis in the Italian scenario, International Journal of Hydrogen Energy (2020).

[20] M. Rivarolo, O. Improta, L. Magistri, M. Panizza, A. Barbucci, Thermoeconomic analysis of a hydrogen production system by sodium borohydride (NaBH4), International Journal of Hydrogen Energy 43 (3) (2018) 1606–1614.

[21] M. Mohsin, A. Rasheed, R. Saidur, Economic viability and production capacity of wind generated renewable hydrogen, International Journal of hydrogen energy 43 (5) (2018) 2621–2630.

[22] T. Ayodele, J. Munda, Potential and economic viability of green hydrogen production by water electrolysis using wind energy resources in South Africa, International Journal of Hydrogen Energy 44 (33) (2019) 17669–17687.

[23] G. Mavromatidis, K. Orehounig, J. Carmeliet, A review of uncertainty characterisation approaches for the optimal design of distributed energy systems, Renewable and Sustainable Energy Reviews 88 (2018) 258–277.

[24] B. Liu, Y. Wang, Energy system optimization under uncertainties: A comprehensive review, Towards Sustainable Chemical Processes (2020) 149–170.

[25] G. B. Dantzig, Linear programming under uncertainty, Management science 1 (3-4) (1955) 197–206.

[26] A. Zakaria, F. B. Ismail, M. H. Lipu, M. A. Hannan, Uncertainty models for stochastic optimization in renewable energy applications, Renewable Energy 145 (2020) 1543–1571.

[27] A. Ben-Tal, L. El Ghaoui, A. Nemirovski, Robust optimization, Princeton university press, 2009.

[28] V. Penadés-Plà, T. Garcia-Segura, V. Yepes, Robust design optimization for low-cost concrete box-girder bridge, Mathematics 8 (3) (2020) 398.

[29] T. Ghisu, J. P. Jarrett, G. T. Parks, Robust design optimization of airfoils with respect to ice accretion, Journal of Aircraft 48 (1) (2011) 287–304.

[30] T. Chatterjee, S. Chakraborty, R. Chowdhury, A Critical Review of Surrogate Assisted Robust Design Optimization, Archives of Computational Methods in Engineering (2017) 1–30.

[31] H. Yu, Reliability-based design optimization of structures: methodologies and applications to vibration control, Ph.D. thesis, Ecully, Ecole centrale de Lyon (2011).

[32] Z. Kang, Robust design optimization of structures under uncertainties (2005).

[33] N. Bilel, N. Mohamed, A. Zouhaier, R. Lotfi, Multi-objective robust design optimization of a mechatronic system with uncertain parameters, using a polynomial chaos expansion method, Proceedings of the Institution of Mechanical Engineers, Part I: Journal of Systems and Control Engineering 231 (9) (2017) 729–739.

[34] W. De Paepe, D. Coppitters, S. Abraham, P. Tsirikoglou, G. Ghorbaniasl, F. Contino, Robust Operational Optimization of a Typical micro Gas Turbine, Energy Procedia 158 (2019) 5795–5803.

[35] A. Younesi, H. Shayeghi, A. Safari, P. Siano, Assessing the resilience of multi microgrid based widespread power systems against natural disasters using Monte Carlo Simulation, Energy 207 (2020) 118220.

[36] K. Verleysen, A. Parente, F. Contino, How sensitive is a dynamic ammonia synthesis process? Global sensitivity analysis of a dynamic Haber-Bosch process (for flexible seasonal energy storage), Energy (2021) 121016.

[37] B. Sudret, S. Marelli, J. Wiart, Surrogate models for uncertainty quantification: An overview, in: 2017 11th European conference on antennas and propagation (EUCAP), IEEE, 2017, pp. 793–797.

[38] Z. Deng, X. Hu, X. Lin, Y. Che, L. Xu, W. Guo, Data-driven state of charge estimation for lithium-ion battery packs based on Gaussian process regression, Energy 205 (2020) 118000.

[39] P. Tsirikoglou, S. Abraham, F. Contino, C. Lacor, G. Ghorbaniasl, A hyperparameters selection technique for support vector regression models, Applied Soft Computing 61 (2017) 139–148.

[40] B. Sudret, Polynomial chaos expansions and stochastic finite-element methods, Risk and Reliability in Geotechnical Engineering Chap. 6 (2003) (2014) 265–300.

[41] K. Verleysen, D. Coppitters, A. Parente, W. De Paepe, F. Contino, How can power-to-ammonia be robust? Optimization of an ammonia synthesis plant powered by a wind turbine considering operational uncertainties, Fuel 266 (2020) 117049.

[42] D. Coppitters, W. De Paepe, F. Contino, Surrogate-assisted robust design optimization and global sensitivity analysis of a directly coupled photovoltaic-electrolyzer system under techno-economic uncertainty, Applied Energy 248 (2019) 310–320.

[43] G. Blatman, B. Sudret, Adaptive sparse polynomial chaos expansion based on least angle regression, Journal of Computational Physics 230 (6) (2011) 2345–2367.

[44] S. Abraham, M. Raisee, G. Ghorbaniasl, F. Contino, C. Lacor, A robust and efficient stepwise regression method for building sparse polynomial chaos expansions, Journal of Computational Physics 332 (2017) 461–474.

[45] D. Coppitters, W. De Paepe, F. Contino, Robust design optimization and stochastic performance analysis of a grid-connected photovoltaic system with battery storage and hydrogen storage, Energy 213 (2020) 118798.

[46] Available online: `https://www.delijn.be/nl/overdelijn/organisatie/geschiedenis/`. Accessed: 16th February 2021.

[47] B. Reuter, M. Faltenbacher, O. Schuller, N. Whitehouse, New Bus ReFuelling for European Hydrogen Bus Depots - Guidance Document on Large Scale Hydrogen Bus Refuelling, Tech. rep., Fuel Cells and Hydrogen, Joint Undertaking (2017).

[48] A. Buttler, H. Spliethoff, Current status of water electrolysis for energy storage, grid balancing and sector coupling via power-to-gas and power-to-

liquids: A review, Renewable and Sustainable Energy Reviews 82 (2018) 2440–2454.

[49] B. E. carbon reduction in business, Update on the digital meter and grid tariffing methodology in Flanders, Tech. rep., Interreg 2 Seas Mers Zeeën - European Regional Development Fund (2018).

[50] W. F. Holmgren, C. W. Hansen, M. A. Mikofski, pvlib python: a python package for modeling solar energy systems, The Journal of Open Source Software 3 (2018) 884.

[51] T. Gurupira, A. Rix, Pv simulation software comparisons: Pvsyst, nrel sam and pvlib, in: Conf.: SAUPEC, 2017.

[52] D. Coppitters, W. De Paepe, F. Contino, Robust design optimization of a photovoltaic-battery-heat pump system with thermal storage under aleatory and epistemic uncertainty, Energy (2021) 120692.

[53] I. Staffell, S. Pfenninger, Using bias-corrected reanalysis to simulate current and future wind power output, Energy 114 (2016) 1224–1239.

[54] N. Boccard, Capacity factor of wind power realized values vs. estimates, Energy Policy 37 (7) (2009) 2679–2688.

[55] Z. Abdin, C. J. Webb, E. M. Gray, Modelling and simulation of a proton exchange membrane (PEM) electrolyser cell, International Journal of Hydrogen Energy 40 (39) (2015) 13243–13257.

[56] F. Marangio, M. Pagani, M. Santarelli, M. Cali, Concept of a high pressure PEM electrolyser prototype, International Journal of Hydrogen Energy 36 (13) (2011) 7807–7815.

[57] Monterey Gardiner, Hydrogen and Fuel Cells Program Record 9013: Energy requirements for hydrogen gas compression and liquefaction as related to vehicle storage needs, Tech. rep. (2019).

[58] B. Zakeri, S. Syri, Electrical energy storage systems: A comparative life cycle cost analysis, Renewable and sustainable energy reviews 42 (2015) 569–596.

[59] Elia, Electricity scenarios for Belgium towards 2050: Elia's quantified study on the energy transition in 2030 and 2040, Tech. rep., Elia (2017).

[60] I. Duić, N. Štefanić, Z. Lulić, G. Krajačić, T. Pukšec, T. Novosel, EU28 fuel prices for 2015, 2030 and 2050. Deliverable 6.1: Future fuel price review (2017).

[61] H. C. Frey, N. M. Rouphail, H. Zhai, T. L. Farias, G. A. Gonçalves, Comparing real-world fuel consumption for diesel-and hydrogen-fueled transit buses and implication for emissions, Transportation Research Part D: Transport and Environment 12 (4) (2007) 281–291.

[62] United Nations Framework Convention for Climate Change., National emissions reported to the UNFCCC and to the EU Greenhouse Gas Monitoring Mechanism (2020).

[63] S. Wilcox, W. Marion, Users manual for TMY3 data sets, Tech. rep., National Renewable Energy Laboratory Golden, CO (2008).

[64] K. Deb, A. Pratap, S. Agarwal, T. Meyarivan, A fast and elitist multiobjective genetic algorithm: NSGA-II, IEEE Transactions on Evolutionary Computation 6 (2) (2002) 182–197.

[65] P. Tsirikoglou, S. Abraham, F. Contino, Ö. Bağci, J. Vierendeels, G. Ghorbaniasl, Comparison of metaheuristics algorithms on robust design optimization of a plain-fin-tube heat exchanger, in: 18th AIAA/ISSMO Multidisciplinary Analysis and Optimization Conference, 2017, p. 3827.

[66] S. Giorgetti, D. Coppitters, F. Contino, W. D. Paepe, L. Bricteux, G. Aversano, A. Parente, Surrogate-Assisted Modeling and Robust Optimization of a Micro Gas Turbine Plant With Carbon Capture, Journal of Engineering for Gas Turbines and Power 142 (1) (2020).

[67] M. Stein, Large sample properties of simulations using latin hypercube sampling, Technometrics 29 (2) (1987) 143–151.

[68] M. Gökçek, C. Kale, Techno-economical evaluation of a hydrogen refuelling station powered by Wind-PV hybrid power system: A case study for İzmir-Çeşme, International Journal of Hydrogen Energy 43 (23) (2018) 10615–10625.

[69] S. M. Wilcox, National solar radiation database 1991-2010 update: User's manual, Tech. rep., National Renewable Energy Lab.(NREL), Golden, CO (United States) (2012).

[70] Triami Media BV, Historic inflation Belgium - CPI inflation, Available online: `inflation.eu/inflation-rates/belgium/historic-inflation/cpi-inflation-belgium.aspx`. Accessed: 1st August 2020 (2019).

[71] International Energy Agency, Renewables 2019: Analysis and forecast to 2024, Tech. rep., International Energy Agency (2019).

[72] L. Reichenberg, F. Hedenus, M. Odenberger, F. Johnsson, The marginal system LCOE of variable renewables – Evaluating high penetration levels of wind and solar in Europe, Energy 152 (2018) 914–924.

[73] T. F. Kristjansdottir, C. S. Good, M. R. Inman, R. D. Schlanbusch, I. Andresen, Embodied greenhouse gas emissions from pv systems in norwegian residential zero emission pilot buildings, Solar Energy 133 (2016) 155–171.

[74] R. H. Wiser, M. Bolinger, 2018 wind technologies market report (2019).

[75] E. A. Smoucha, K. Fitzpatrick, S. Buckingham, O. G. Knox, Life cycle analysis of the embodied carbon emissions from 14 wind turbines with rated powers between 50kW and 3.4 MW, Journal of Fundamentals of Renewable Energy and Applications 6 (4) (2016) 1000211.

[76] B. Guinot, B. Champel, F. Montignac, E. Lemaire, D. Vannucci, S. Sailler, Y. Bultel, Techno-economic study of a PV-hydrogen-battery hybrid system

for off-grid power supply: Impact of performances' ageing on optimal system sizing and competitiveness, International Journal of Hydrogen Energy 40 (1) (2015) 623–632.

[77] W. G. Colella, B. D. James, J. M. Moton, G. Saur, T. Ramsden, Techno-economic Analysis of PEM Electrolysis for Hydrogen Production, Tech. rep., Strategic Analysis inc. and National Renewable Energy Laboratory (NREL) (2014).

[78] X. Zhang, C. Bauer, C. L. Mutel, K. Volkart, Life Cycle Assessment of Power-to-Gas: Approaches, system variations and their environmental implications, Applied Energy 190 (2017) 326–338.

[79] A. Mayyas, M. Mann, Manufacturing competitiveness analysis for hydrogen refueling stations, International Journal of Hydrogen Energy 44 (18) (2019) 9121–9142.

[80] Y. Zhang, P. E. Campana, A. Lundblad, J. Yan, Comparative study of hydrogen storage and battery storage in grid connected photovoltaic system: Storage sizing and rule-based operation, Applied Energy 201 (2017) 397–411.

[81] International Stainless Steel Forum, Stainless Steel and CO2: Facts and Scientific Observations, Tech. rep. (2019).

[82] S. Niaz, T. Manzoor, A. H. Pandith, Hydrogen storage: Materials, methods and perspectives, Renewable and Sustainable Energy Reviews 50 (2015) 457–469.

[83] W. K. Biswas, V. Duong, P. Frey, M. N. Islam, A comparison of repaired, remanufactured and new compressors used in Western Australian small-and medium-sized enterprises in terms of global warming, Journal of Remanufacturing 3 (1) (2013) 1–7.

[84] Civitas, Smart Choices for Cities—Clean Buses for Your City, Police Note 52 (2013).

[85] Y. Ruf, M. Kaufmann, S. Lange, J. Pfister, F. Heieck, A. Endres, Fuel Cells and Hydrogen Applications for Regions and Cities, Roland Berger: Brussels, Belgium (2017).

[86] N. Pocard, C. Reid, Fuel cell electric buses: An attractive value proposition for zero-emission buses in the united kingdom, Balard: London, UK (2016).

[87] Z. Liu, T. Li, Q. Jiang, H. Zhang, Life cycle assessment–based comparative evaluation of originally manufactured and remanufactured diesel engines, Journal of Industrial Ecology 18 (4) (2014) 567–576.

[88] R. Kawamoto, H. Mochizuki, Y. Moriguchi, T. Nakano, M. Motohashi, Y. Sakai, A. Inaba, Estimation of CO2 Emissions of internal combustion engine vehicle and battery electric vehicle using LCA, Sustainability 11 (9) (2019) 2690.

[89] S. Dhanushkodi, N. Mahinpey, A. Srinivasan, M. Wilson, Life cycle analysis of fuel cell technology, Journal of Environmental Informatics 11 (1) (2008) 36–44.

[90] R. Fu, D. J. Feldman, R. M. Margolis, US solar photovoltaic system cost benchmark: Q1 2018, Tech. rep., National Renewable Energy Lab.(NREL), Golden, CO (United States) (2018).

[91] T. Mayer, M. Semmel, M. A. G. Morales, K. M. Schmidt, A. Bauer, J. Wind, Techno-economic evaluation of hydrogen refueling stations with liquid or gaseous stored hydrogen, International Journal of Hydrogen Energy 44 (47) (2019) 25809–25833.

[92] R. P. Micena, O. R. Llerena-Pizarro, T. M. de Souza, J. L. Silveira, Solar-powered Hydrogen Refueling Stations: A techno-economic analysis, International Journal of Hydrogen Energy 45 (3) (2020) 2308–2318.

[93] I. Iordache, D. Schitea, M. Iordache, Hydrogen refueling station infrastructure roll-up, an indicative assessment of the commercial viability and

profitability, International Journal of Hydrogen Energy 42 (8) (2017) 4721–4732.

[94] Ø. Ulleberg, R. Hancke, Techno-economic calculations of small-scale hydrogen supply systems for zero emission transport in norway, international journal of hydrogen energy 45 (2) (2020) 1201–1211.